journal

J. Am. Ceram. Soc., 92 [3] 694–701 (2009)
DOI: 10.1111/j.1551-2916.2008.02914.x
© 2009 The American Ceramic Society

Relationship Between Engineering Properties, Mineralogy, and Microstructure in Cement-Based Hydroceramic Materials Cured at 200°–350°C

Konstantinos Kyritsis,[‡†] Christopher Hall,[‡] Dale P. Bentz,[§] Nicola Meller,[‡] and Moira A. Wilson[¶]

[‡]Centre for Science at Extreme Conditions and School of Engineering & Electronics, The University of Edinburgh, The King's Buildings, Edinburgh EH9 3JL, U.K.

[§]Building and Fire Research Laboratory, National Institute of Standards and Technology, Gaithersburg, Maryland 20899

[¶]School of Mechanical, Aerospace and Civil Engineering, The University of Manchester, Manchester M60 1QD, U.K.

Cement-based materials used to seal geothermal or deep oil wells are exposed to severe conditions. Optimizing engineering properties such as strength and permeability is therefore very important. We have synthesized hydroceramic materials for such applications based on the $CaO-Al_2O_3-SiO_2-H_2O$ (CASH) system and cured them over a range of temperatures (200°–350°C). Depending on initial composition and curing temperature, hydroceramics of complex and diverse mineralogy and microstructure are formed. The minerals found include portlandite, jaffeite, xonotlite, gyrolite, 11 Å tobermorite, truscottite, hydrogarnet, and calcium aluminum silicate hydrate. These cement-based hydroceramic materials develop complicated pore structures, which strongly affect bulk properties. We report the compressive strength and permeability of these materials and show how these bulk engineering properties are related to microstructure. The compressive strength was found to be in the range 2–52 MPa and the intrinsic permeability in the range 0.5×10^{-17} to 3300×10^{-17} m^2. Scanning electron microscopy (SEM) was used for imaging the hydroceramic microstructures. Further, we have computed the intrinsic permeability from 2-D SEM images by using the Stokes equation solver, Permsolver, applied to reconstructed 3-D images and the results are shown to be in good agreement with experimentally determined values.

I. Introduction

Cement is universally used in the construction of oil and geothermal wells. Cement slurries are placed primarily to secure and support the casing inside the well, but also to prevent entry of unwanted fluids into the well and communication between formation fluids at different levels.[1] These cements need to perform for many years at high temperatures and in severe chemical environments, such as in brines or in ground waters containing carbon dioxide.[2] Such environments can cause the material of the well casing to degrade causing reduced strength and increased permeability.[3–6] It is therefore necessary for cement formulations to be sufficiently durable and resistant to chemical attack to seal the well for its working life.

Typical working temperatures for these wells are between 200° and 350°C and as the temperature greatly exceeds 110°C special cement formulations are used.[1] There have been several recent attempts to design cements that are more durable at higher temperatures. Meller *et al.*[7–10] have designed slurries based on the $CaO-Al_2O_3-SiO_2-H_2O$ (CASH) system, with the aim of developing formulations suitable for geothermal and deep, hot oil wells. These formulations contain minerals that occur in nature and hence have the potential properties required to be good well sealants, i.e. low permeability, high strength, and long-term stability. The mineralogy and the quantification of the phases present in this system are described in detail elsewhere.[10]

The physical properties of cementitious materials required for such applications have been investigated previously[1,11–18] and it is considered that the minimum compressive strength of the hardened slurry should be at least 7 MPa and the maximum permeability approximately 9×10^{-17} m^2 (1×10^{-9} m/s or 0.1 mD).[19] Although some work has been carried out on the mechanical properties of cement-based well sealants, little is known about the relationship between the bulk properties and the microstructure of the materials. This is addressed here with respect to the CASH hydroceramic system; in addition the measured permeability of real samples is compared with that calculated from microstructural information.

II. Experimental Procedure

Three reagents were used in the synthesis of the hydroceramic materials described here. Dyckerhoff oilwell cement (API Class G)[‖] was the base component in all samples. This cement is widely used in practice and has a consistent composition. The oxide analysis of the cement and the calculated mineralogical composition are given in Table I. Silica flour (HPF6 supplied by Sibelco) with a mean grain size of 53 μm and α-alumina (corundum, supplied by Sigma Aldrich, Gillingham, Dorset, SP8 4XT, U.K.) with a grain size of 50–150 μm were used as the sources of SiO_2 and Al_2O_3, respectively. Silica and alumina were added to the base mixtures at various mass percentages (designated simply as % from this point forward).

Two different-sized specimens were made. To examine compressive strength, cylindrical polytetrafluoroethylene (PTFE) cups were used, 22 mm in diameter and 45 mm deep. For permeability measurements smaller cups were used of the same diameter but only 30 mm deep. A total of 30 g of the three starting materials was weighed out in different proportions (Table II) and 12 g of water added corresponding to a water:solids ratio of 0.4. Each sample was mixed by hand for approximately 3 min

H. Jennings—contributing editor

Manuscript No. 25171. Received August 29, 2008; approved November 24, 2008.
This work was supported by the Engineering and Physical Sciences Research Council, U.K., under Grant No. GR/T18998/01
[†]Author to whom correspondence should be addressed. e-mail: k.kyritsis@ed.ac.uk

[‖]Certain commercial products are identified in this paper to specify the materials used and procedures used. In no case does such identification imply endorsement or recommendation by the National Institute of Standards and Technology, nor does it indicate that the products are necessarily the best available for the purpose.

Table I. Chemical Composition of Dyckerhoff Class G cement Determined by X-Ray Fluorescence and LECO Sulfur Analysis

Oxides	Mass%
Na_2O	0.17
MgO	0.76
Al_2O_3	3.62
SiO_2	22.55
K_2O	0.66
CaO	65.61
TiO_2	0.17
Mn_3O_4	0.14
Fe_2O_3	4.53
SO_3	1.82
Loss on ignition at 1000°C	1.18
Free lime	0.40
Insoluble residue	Not determined

and then loaded into the appropriate cup. For the samples cured at 350°C, stainless-steel cups were used, as PTFE was close to its melting point. The samples were stacked in a stainless-steel autoclave cell of 125 mL capacity with a pressure rating of 2×10^7 Pa at the maximum working temperature of 350°C. Small notches were cut in the rims of the PTFE and steel cups to ensure a uniform water-saturated atmosphere throughout the vessel. Once the cells were sealed, they were placed in the oven at the selected curing temperature in the range of 200°–350°C and left to equilibrate for 5 days. After curing, the cells were removed from the oven and left to cool down slowly to prevent the samples cracking. Samples were then left to dry in a vacuum to reduce carbonation before they were removed from the cups.

The mineralogy was determined by quantitative X-ray diffraction using Rietveld refinement. Details of the equipment used are provided elsewhere.[10]

Compressive strength was measured using a 50 kN mechanical testing machine. Compressive tests were carried out in accordance with the American Society for Testing and Materials (ASTM) C39-96[20] on samples with an aspect ratio of 2 (44 mm length and 22 mm diameter). The sample was loaded at a displacement rate of 0.33 mm/min. Three samples of each composition were tested to check reproducibility. A typical coefficient of variation between triplicate specimens for compressive strength measurements was 0.1. The compressive strength was determined from the applied load at the point of sample failure.

Table II. Proportions (Mass%) of Starting Materials in Samples Cured at 200°, 250°, 300°, and 350°C

Dyckerhoff cement	Silica flour HPF6	α-alumina
100	0	0
90	10	0
80	20	0
70	30	0
60	40	0
50	50	0
90	0	10
80	0	20
70	0	30
60	0	40
50	0	50
80	10	10
60	10	30
60	20	20
60	30	10
50	10	40
50	40	10

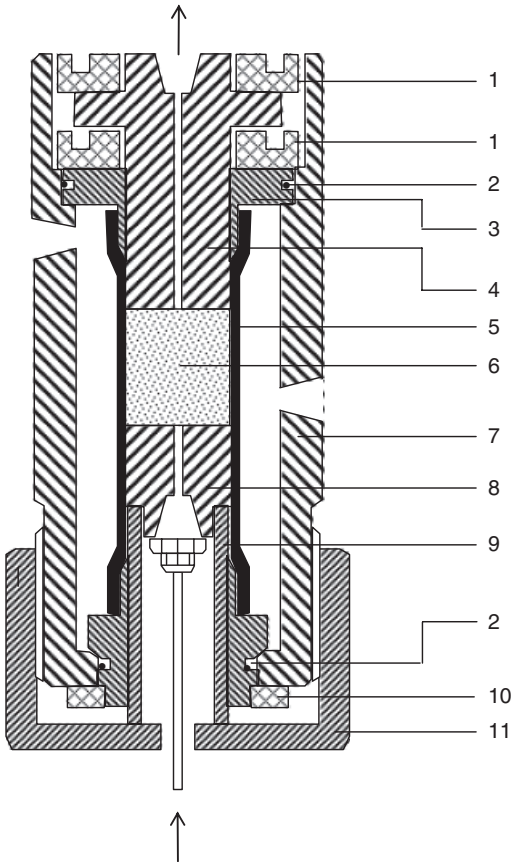

Fig. 1. Hassler cell permeameter after Hall and Hoff[26]: 1, retaining ring; 2, nitrile rubber O-ring seal and PTFE back-up ring; 3, sleeve carrier; 4, fixed platen; 5, nitrile rubber sleeve; 6, sample; 7, stainless-steel case; 8, movable platen; 9, platen carrier; 10, retaining ring; 11, end cap.

There are several methods of measuring the permeability of cement-based materials.[21,22] The permeability results reported here were obtained using a purpose-built Hassler cell permeameter. This type of cell is widely used in petroleum technology[23] and, more recently, has been used in measurements of the permeability of construction materials[24] and in the extraction of pore solution from cement materials.[25] A schematic diagram of the Hassler cell is shown in Fig. 1 and a full description of the technique and associated equipment is given by Green *et al.*[27] In brief, the Hassler cell is an axial flow permeameter designed to measure the satiated permeability of cylindrical specimens of $\approx$25 mm diameter and between 25 and 75 mm in length. Before measurement, the specimen must be saturated with the test liquid, in this case deionized water. The specimen is placed inside a nitrile rubber sleeve to which a containing pressure is applied that exceeds the pressure of the liquid flowing through the sample. This containing pressure, which is monitored by a pressure transducer, seals the circumferential face of the sample and ensures axial flow. A constant flow of liquid through the sample is provided by a pulse-free chromatography pump and the pressure necessary to maintain this flow, the fluid pressure, is monitored by a second pressure transducer. Darcian flow through the sample is confirmed by an increase in flow rate resulting in a directly proportional increase in fluid pressure.

Permeability test specimens, 22 mm diameter × 30 mm length, were vacuum saturated with deionized water before being loaded into the Hassler cell. The containing pressure was maintained at 5 MPa for samples having a compressive strength >10 MPa and at 2.5 MPa for those with a compressive strength <10 MPa. The saturated liquid conductivity (or intrinsic permeability), K, was calculated from the equation $K = QL/PA$ where Q is the steady volumetric flow rate through the sample of length L and cross-sectional area A at inlet gauge pressure P. A typical

Table III. Phases Identified in Each Sample as Estimated by Rietveld Refinement

Proportions (mass%)						
Dyckerhoff cement	SiO_2	α-Al_2O_3	200°C	250°C	300°C	350°C
100	0	0	$p = 8$; $j = 74$; $a = 18$	$p = 5$; $j = 76$; $r = 19$	$p = 14$; $j = 36$; $r = 34$; $h = 16$	$p = 18$; $j = 20$; $r = 47$; $h = 15$
90	10	0	$j = 9$; $a = 6$; $m = 49$; $k = 27$; $t = 9$	$j = 2$; $r = 6$; $m = 84$; $x = 8$	$j = 2$; $r = 11$; $m = 74$; $x = 12$	$j = 10$; $r = 68$; $f = 8$; $h = 14$
80	20	0	$j = 1$; $m = 37$; $k = 10$; $t = 16$; $x = 31$	$m = 82$; $x = 18$	$m = 73$; $x = 27$	$x = 100$
70	30	0	$t = 8$; $x = 92$	$x = 100$	$x = 98$; $v = 2$	$x = 60$; $v = 40$
60	40	0	$x = 36$; $g = 59$; $q = 6$	$x = 18$; $g = 56$; $v = 26$	$x = 35$; $v = 65$	$x = 10$; $v = 90$
50	50	0	$g = 70$; $q = 30$	$g = 64$; $v = 21$; $q = 21$	$v = 88$; $q = 12$	$v = 84$; $q = 16$
90	0	10	$p = 6$; $j = 30$; $h = 64$	$p = 5$; $j = 8$; $r = 7$; $h = 87$	$p = 7$; $j = 17$; $h = 76$	$p = 12$; $j = 6$; $h = 82$
80	0	20	$j = 3$; $h = 97$	$j = 7$; $h = 92$	$j = 6$; $h = 83$; $d = 11$	$p = 1$; $j = 3$; $h = 72$; $b = 4$; $d = 10$
70	0	30	$j = 3$; $h = 80$; $c = 16$	$j = 8$; $h = 75$; $c = 16$	$j = 5$; $h = 67$; $c = 11$; $d = 16$	$h = 56$; $c = 13$; $b = 11$; $d = 20$
60	0	40	$j = 3$; $h = 73$; $c = 30$	$j = 6$; $h = 62$; $c = 32$	$j = 4$; $h = 47$; $c = 31$; $d = 18$	$h = 43$; $c = 29$; $b = 10$; $d = 18$
50	0	50	$j = 2$; $h = 60$; $c = 43$	$j = 5$; $h = 51$; $c = 44$	$j = 3$; $h = 44$; $c = 42$; $d = 11$	$h = 35$; $c = 42$; $b = 8$; $d = 15$
80	10	10	$j = 7$; $k = 26$; $t = 12$; h = 49; $c = 6$	$j = 11$; $h = 89$	$j = 7$; $h = 93$	$p = 1$; $j = 4$; $x = 18$; $f = 1$; $h = 75$
60	10	30	$j = 1$; $t = 8$; $h = 68$; $c = 23$	$t = 6$; $h = 67$; $c = 27$	$h = 83$; $c = 19$	$x = 4$; $h = 73$; $c = 20$; $b = 4$
60	20	20	$t = 18$; $x = 36$; $h = 26$; $c = 20$	$t = 7$; $x = 40$; $h = 34$; $c = 19$	$x = 45$; $h = 33$; $c = 21$	$x = 56$; $h = 14$; $c = 30$
60	30	10	$t = 19$; $x = 64$; $h = 5$; $c = 12$	$x = 84$; $c = 16$	$x = 55$; $v = 31$; $c = 13$	$x = 21$; $v = 58$; $h = 6$; $c = 14$
50	10	40	$t = 9$; $h = 54$; $c = 36$	$t = 4$; $x = 10$; $h = 48$; $c = 38$	$x = 3$; $h = 63$; $c = 33$	$h = 65$; $c = 32$; $b = 2$
50	40	10	$g = 83$; $q = 8$; $c = 9$	$g = 64$; $v = 20$; $q = 4$; $c = 12$	$x = 13$; $v = 71$; $q = 2$; $c = 15$	$x = 4$; $v = 76$; $q = 6$; $c = 14$

Codes for phases: *a*, α-dicalcium silicate hydrate (α-$Ca_2SiO_4 \cdot H_2O$); *m*, octacalcium pentasilicate ($Ca_8Si_5O_{15}$); *g*, gyrolite ($Ca_{16}Si_{24}O_{60}(OH)_8 \cdot (14+n)H_2O$); *b*, bicchulite ($Ca_2(Al_2SiO_6)(OH)_2$); *c*, corundum; *d*, calcium aluminate hydrate ($Ca_4Al_6O_{13} \cdot 3H_2O$); *f*, foshagite ($Ca_3(SiO_3)_3(OH)_2$); *h*, hydrogarnet ($Ca_3Al_2(SiO_4)_{3-y}(OH)_{4y}$); *j*, jaffeite ($Ca_6(Si_2O_7)(OH)_6$); *k*, kilchoanite ($Ca_6(SiO_4)(Si_3O_{10})$); *p*, portlandite ($Ca(OH)_2$); *q*, quartz; *r*, reinhardbraunsite ($Ca_5(SiO_4)_2(OH)_2$); *t*, 11 Å tobermorite ($Ca_5Si_6O_{17} \cdot 5H_2O$); *v*, truscottite ($Ca_{14}Si_{24}O_{62} \cdot (4+z)H_2O$); *x*, xonotlite ($Ca_6Si_6O_{17}(OH)_2$).

coefficient of variation between triplicate specimens for permeability measurements was 0.2.

To image the microstructure of the hydroceramic samples, a scanning electron microscope was used with an acceleration voltage of 5 kV. To minimize charging, the samples were sputter coated with approximately 8 nm of 60% gold and 40% palladium.

Finally simulation experiments were carried out to calculate permeability using computer models that are freely available to the public from the National Institute of Standards and Technology (NIST, Gaithersburg, MD, http://ciks.cbt.nist.gov/cmml.html).

III. Results and Discussion

(1) Mineralogy

By adding small amounts of silica flour (<20%) to the cement, jaffeite ($Ca_6(Si_2O_7)(OH)_6$), octacalcium pentasilicate ($Ca_8Si_5O_{15}$), kilchoanite ($Ca_6(SiO_4)(Si_3O_{10})$), α-dicalcium silicate hydrate (α-$Ca_2SiO_4 \cdot H_2O$), and 11 Å tobermorite ($Ca_5Si_6O_{17} \cdot 5H_2O$) form at 200°C. In these samples reinhardbraunsite ($Ca_5(SiO_4)_2(OH)_2$) replaces α-dicalcium silicate hydrate at 250°, 300°, and 350°C. Increasing the amount of silica (>40%) resulted in the formation of xonotlite ($Ca_6Si_6O_{17}(OH)_2$), gyrolite ($Ca_{16}Si_{24}O_{60}(OH)_8 \cdot (14+n)H_2O$, $0<n<3$), and some relict quartz (SiO_2) at 200° and 250°C. At temperatures of 300° and 350°C, truscottite ($Ca_{14}Si_{24}O_{62} \cdot (4+z)H_2O$, $0<z<6$) is formed instead of gyrolite. By adding small amounts of alumina, portlandite ($Ca(OH)_2$) and jaffeite form together with the hydrogarnet phase ($Ca_3Al_2(SiO_4)_{3-y}(OH)_{4y}$, $0<y<3$). In these, samples reinhardbraunsite is also present at 250°C instead of α-dicalcium silicate hydrate that is formed at 200°C. As more alumina is

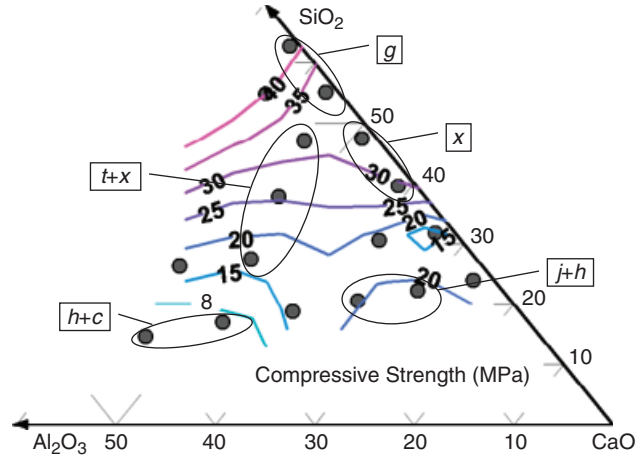

Fig. 2. Ternary contour plot of compressive strength for samples cured at 200°C. Sample points (gray circles) are plotted in molar proportions (per cent) of CaO, SiO_2, and Al_2O_3. Samples in circles indicate the dominant phases in different regions. Codes for phases are shown in Table III.

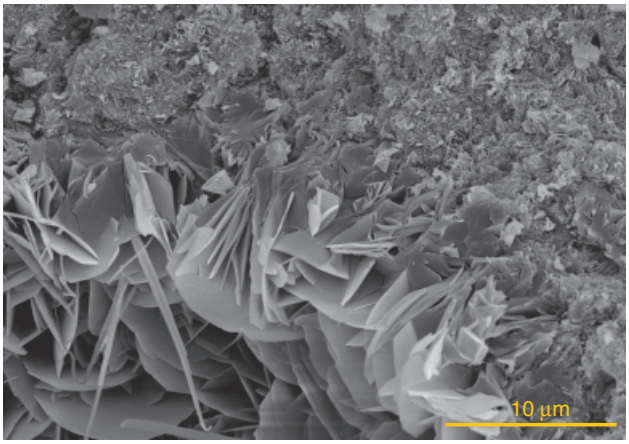

Fig. 3. Scanning electron microscopic (SEM) image illustrating platey crystals of gyrolite growing in sample containing 40% of silica flour cured at 200°C.

added (>20%), jaffeite is the only new phase coexisting with hydrogarnet at 200° and 250°C, together with some relict corundum (Al_2O_3). At 300°C, calcium aluminate hydrate ($Ca_4Al_6O_{13} \cdot 3H_2O$) forms in addition to the phases mentioned previously and at 350°C, bicchulite ($Ca_2(Al_2SiO_6)(OH)_2$) is present (Table III).

When small amounts of silica and alumina are added to cement at 200°C, kilchoanite and tobermorite form, together with jaffeite, hydrogarnet, and corundum. As more silica is added to the system, xonotlite replaces kilchoanite. At 250°C, kilchoanite is not present and only jaffeite, hydrogarnet, tobermorite, xonotlite, and corundum form depending on the proportions of the starting materials (Table III). The same minerals form at 300° and 350°C, the only difference being the absence of tobermorite and the presence of foshagite ($Ca_3(SiO_3)_3(OH)_2$) at 350°C when small amounts of silica and alumina are added. Also truscottite forms instead of gyrolite when adding small amounts of alumina and high amounts of silica flour. As can be seen from Table III, the mineralogy of this system (CASH) is complicated and it is described in more detail elsewhere.[7,9,10] Here we focus on the significance of the different minerals on the engineering properties of these materials.

(2) Compressive Strength

Samples cured at 200° and 250°C have almost the same engineering properties, as their mineralogy is similar (Table III). The ternary contour plot in Fig. 2 shows the compressive strength of the samples cured at 200°C. The sample compositions are expressed as molar proportions of the three major oxides present in the system CaO, SiO_2, and Al_2O_3. The molar proportions of SiO_2 and Al_2O_3 are calculated including the amount of these oxides that cement contains, and the amount added to each sample. When more than 20% of silica only is added to the system at 200°C the strength starts to improve. Xonotlite and 11 Å tobermorite are responsible for this improvement as they grow at the expense of α-dicalcium silicate hydrate, which is known for strength retrogression in cement systems.[1,4] Adding more silica causes platey crystals of gyrolite to form (Fig. 3), further improving the strength that attains a maximum value of 42 MPa. These results are in good agreement with Grabowski and Gillott[28] who studied similar cement slurries. On the other hand, the addition of small amounts of alumina (10%–15%) to the system only slightly improves the strength. The addition of larger proportions of alumina (<20%) causes a decrease in compressive strength. Figure 4(a) shows a sample containing 10% of alumina where needle-shaped crystals of jaffeite form between the hydrogarnet crystals filling the pores and increasing the compressive strength. Once the amount of jaffeite present is significantly decreased (<20%, Table III) hydrogarnet and relict corundum are dominant and the strength is significantly decreased because of increased porosity (Fig. 4(b)). Kalousek[18] also reported that large amounts of hydrogarnet in these systems decrease strength, although his values are higher than those reported here, perhaps because of different mixing compositions and the different curing time used. When both silica and alumina are added at these temperatures, tobermorite forms in addition to hydrogarnet (Table III). Tobermorite is known to improve and stabilize strength in cement-based systems[11,15]; therefore the samples containing this mineral in significant amounts exhibit increased compressive strength as shown in Fig. 2.

The mineralogy of the samples cured at 300°C is similar to that of samples cured at 350°C, and their engineering properties were also similar in terms of compressive strength. Figure 5 illustrates a ternary contour plot of samples cured at 350°C. When adding more than 25% of silica, the compressive strength is increased as xonotlite forms instead of reinhardbraunsite and octacalcium pentasilicate. As more silica is added, hexagonal crystal plates of truscottite form (Fig. 6) increasing strength further to a maximum of 52 MPa. Our results show that samples containing truscottite are stronger than those containing xonotlite, in disagreement with the results of Eilers *et al.*[29] Probably other phases are present apart from truscottite in their system, as their initial cement composition is different from ours, affecting the total strength. On comparing the maximum compressive strength values for samples cured at 200° and 350°C, an increase in strength of approximately 25% is observed as the temperature is increased. This suggests that truscottite, which is formed at higher temperatures (350°C), is stronger than gyrolite that forms at lower temperatures (Table III).

On the other hand, as the amount of alumina in the mix is increased, the compressive strength progressively decreases to a

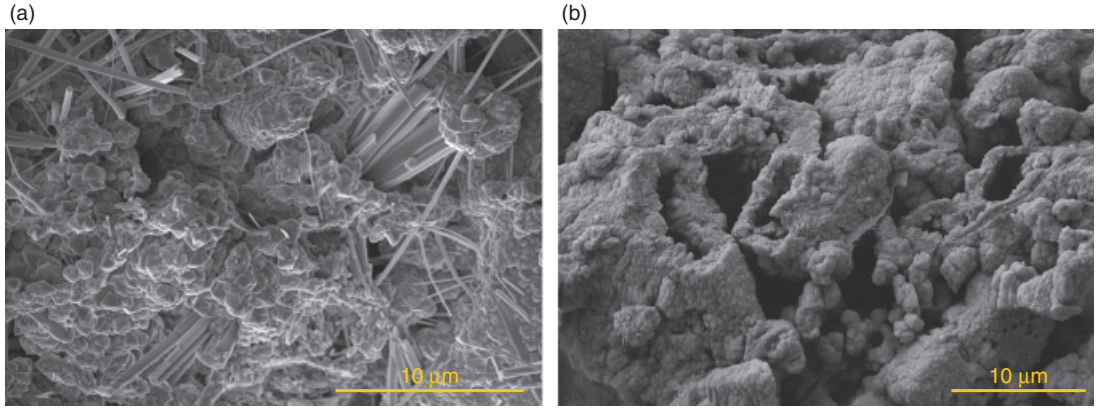

Fig. 4. (a) Scanning electron microscopic (SEM) image showing needle shaped jaffeite crystals growing in the pores between hydrogarnet crystals in sample containing 10% of alumina and cured at 200°C. (b) SEM image of sample cured at 200°C and containing 40% of alumina where only hydrogarnet crystals are present.

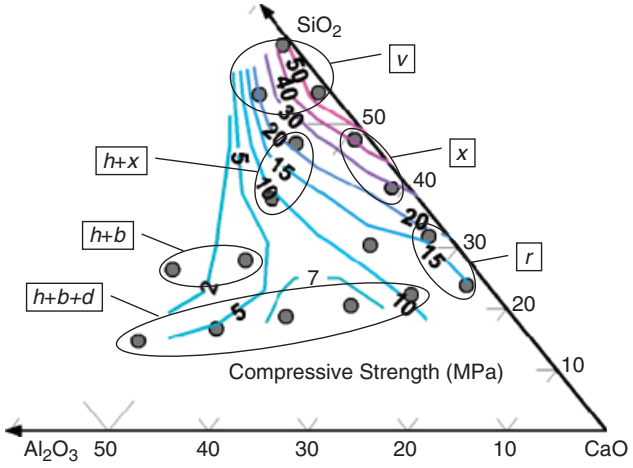

Fig. 5. Ternary contour plot of compressive strength for samples cured at 350°C. Sample points (gray circles) are plotted in molar proportions (per cent) of CaO, SiO_2, and Al_2O_3. Samples in circles indicate the dominant phases in different regions. Codes for phases are shown in Table III.

lowest value of 2 MPa. Apart from hydrogarnets, the formation of two new minerals at these temperatures, calcium alumina silicate hydrate and bicchulite, are responsible for the strength deterioration. Only with both high amounts of silica and low amounts of alumina is the strength increased, since such compositions favor the formation of truscottite. The remaining compositions examined at 300° and 350°C have low strength due to the absence of 11 Å tobermorite.

According to the American Petroleum Institute (API) specifications, the minimum compressive strength required by these materials for use as sealants for very deep oil or geothermal wells is 7 MPa.[19] The hydroceramic samples that meet this criterion are those that contain in large amounts minerals with a Ca/Si ratio of 1 or lower, such as xonotlite, gyrolite, 11 Å tobermorite, and truscottite.

(3) Permeability

The ternary contour plot shown in Fig. 7 illustrates the permeability of the samples cured at 200°C. The pattern of behavior is similar to that of the compressive strength measurements at the same temperature. When silica flour only is added, the permeability is decreased, whereas alumina additions have the reverse effect. The reason for this is the variation in mineralogy as explained in the previous section. When both additives are incorporated, samples containing high amounts of tobermorite exhibit low permeability. Our results are in good agreement

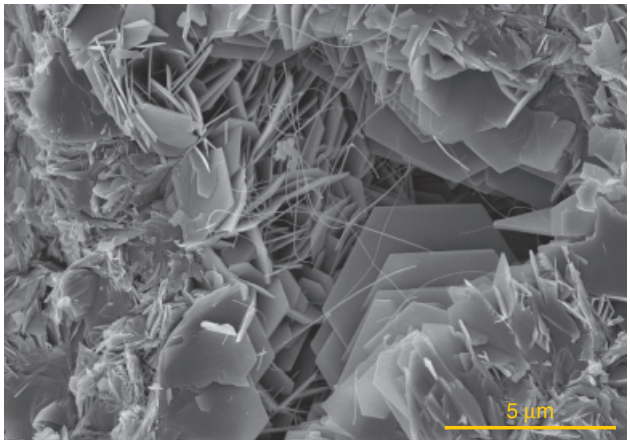

Fig. 6. Scanning electron microscopic (SEM) image showing hexagonal crystals of truscottite. The small needles that are present are of xonotlite. Sample cured at 350°C containing 40% silica flour.

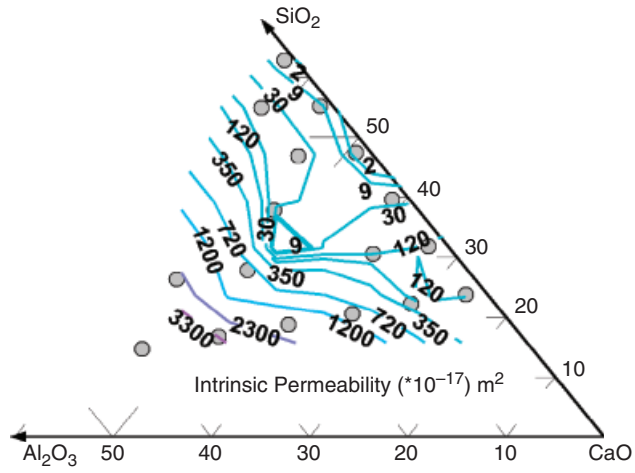

Fig. 7. Ternary contour plot of intrinsic permeability for samples cured at 200°C. Sample points (gray circles) are plotted in molar proportions (per cent) of CaO, SiO_2, and Al_2O_3.

with Nelson *et al.*[30] and Eilers *et al.*,[29] who studied the engineering properties of similar systems at these temperatures.

At higher temperatures (300°–350°C), the permeability behavior in samples containing alumina is different. When adding more than 20% of alumina, the permeability values decrease, as shown in Fig. 8, despite the fact that hydrogarnet is present (Table III). The formation of the two new minerals, calcium aluminum silicate hydrate and bicchulite (Table III), which are present in these samples along with hydrogarnets, are responsible for this. Calcium aluminum silicate hydrate forms platey crystals growing between the hydrogarnet aggregates as shown in Fig. 9, preventing the liquid from moving through the sample, thereby reducing the permeability values. These values meet the API specifications for use as sealants for very deep oil or geothermal wells.

Adding silica flour, the permeability values decrease progressively (Fig. 8). Instead of reinhardbraunsite and octacalcium pentasilicate, xonotlite and truscottite form. Once truscottite is formed (>40% of silica), the values of permeability are the lowest observed in our CASH system. Comparing truscottite with other minerals such as gyrolite, xonotlite, or 11 Å tobermorite, a general improvement of the engineering properties of the hydroceramic materials is observed. Our experiments showed that truscottite is very stable in closed systems, although it is believed that it may be difficult to produce and to maintain in a geothermal environment.[31]

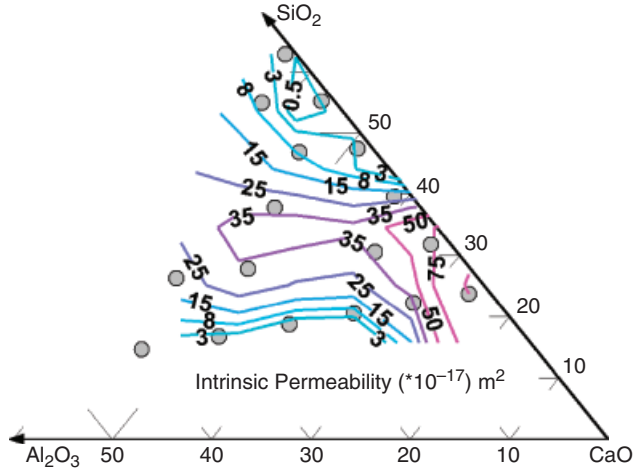

Fig. 8. Ternary contour plot of intrinsic permeability for samples cured at 350°C. Sample points (gray circles) are plotted in molar proportions (per cent) of CaO, SiO_2, and Al_2O_3.

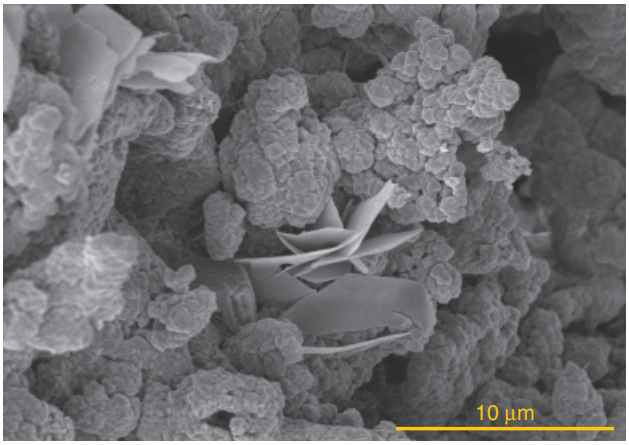

Fig. 9. Scanning electron microscopic (SEM) image illustrating platey crystals of calcium aluminum silicate hydrate growing between hydrogarnet particles in sample containing 30% of alumina cured at 300°C.

When adding both silica and alumina to the samples, a decrease in permeability is observed when truscottite is formed in large amounts (Table III). Although when calcium aluminum silicate hydrate or xonotlite is formed, and depending on the composition of the starting materials, permeability decreases compared with neat cement. In general, the permeability behavior of the system at 300° and 350°C is improved compared with those at lower temperatures. The combination of phases with different crystal shapes produces complicated nonconnected pore structures, hence forming a barrier to liquid penetration.

(4) Permeability Simulation

To simulate permeability, microstructure models closely related to the microstructure of real-hydroceramic samples have been reconstructed using two-dimensional (2-D) SEM images of the real samples. An example of a three-dimensional (3-D) model microstructure generated from a 2-D image is given in Fig. 10. The SEM image of a sample cured at 350°C with 40% addition of silica flour in Fig. 10(a) shows hexagonal truscottite crystals and xonotlite needles. This image has been used as the binary image, after segmentation (Fig. 10(b)), to extract the correlation functions to reconstruct the 3-D microstructure. The final 3-D microstructure generated (Fig. 10(c)) consists of a 3-D grid (lattice) in which each site is defined to be either solid (white) or pore (black). In our study, the lattices were always $100 \times 100 \times 100$ units for a total of one million sites (voxels) with voxel dimensions ranging from 0.25 to 1.95 µm, depending on the specific microstructure being simulated. Porosities for the reconstructed microstructures were set to match those of the physical specimens, which ranged between 25% and 40% for the materials examined in this study. The method used to reconstruct a 3-D porous medium from a 2-D image is fully described by Bentz and Martys.[32] One assumption of the 3-D reconstruction technique is that the pore structure of the real (and reconstructed) microstructure is isotropic.[32] While the individual crystals comprising the solid phases in these microstructures may be highly anisotropic (as seen in Fig. 10(a)), the pore space between them can still be isotropic as indicated by the black regions in the binary image in Fig. 10(b). The reconstruction algorithm generates 3-D porous microstructures with a percolation threshold (equivalent to zero permeability) near 10% porosity,[32] well below the porosity values examined in this study.

Using this 3-D model, the permeability is then calculated using a linear Stokes solver.[33,34] The permeability computer program applies pressure in one of the three principal directions of the 3-D microstructure and computes the resulting velocity vector field within the porosity. Darcy equation[26,34] is then used to calculate the equivalent permeability for the microstructure. The Permsolver permeability codes, have been validated previously by computing the permeabilities of both circular and square tubes.[33] For a square tube 25 units on one side, the error between computed and theoretical permeabilities was only 0.01%, whereas for a circular tube with a diameter of 25 units it was <2%. The codes, together with a user's manual, are

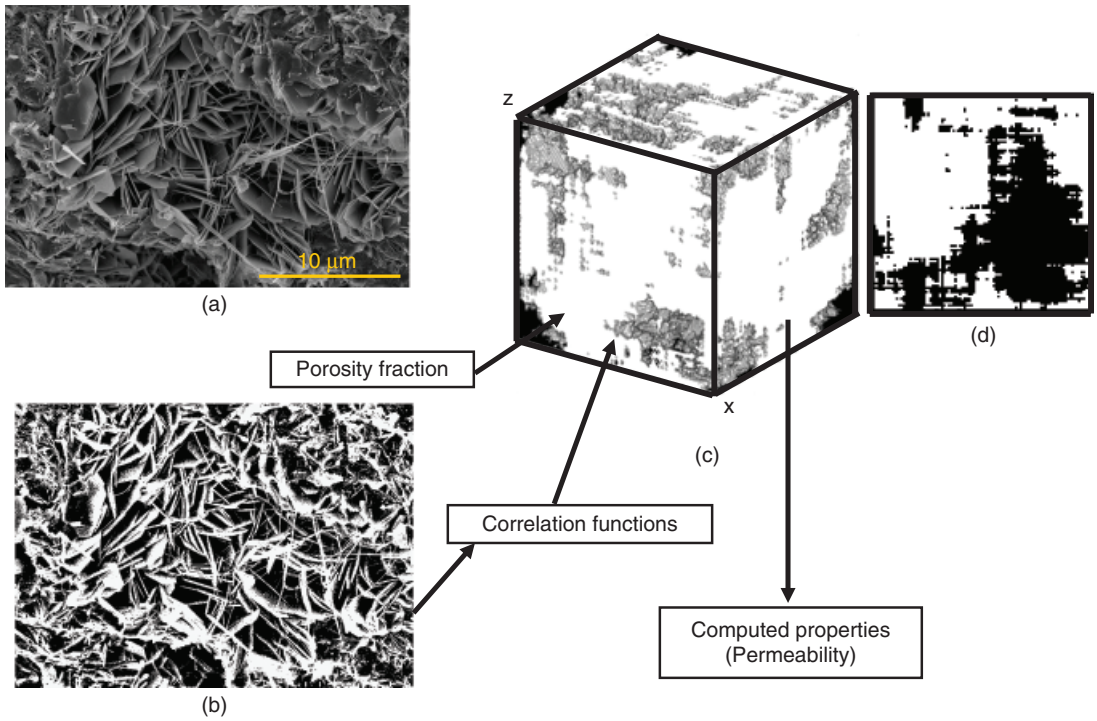

Fig. 10. Illustration of the process of creating a three dimensional microstructure. (a) Scanning electron microscopic (SEM) image showing hexagonal crystals of truscottite. The needle-shaped crystals are of xonotlite. Sample cured at 350°C containing 40% of silica flour. (b) Binary image used to extract the correlation functions for the three-dimensional reconstruction. (c) Reconstructed three-dimensional microstructure ($100 \times 100 \times 100$ pixels) from which permeability is computed. (d) Slice of the reconstructed three dimensional microstructure.

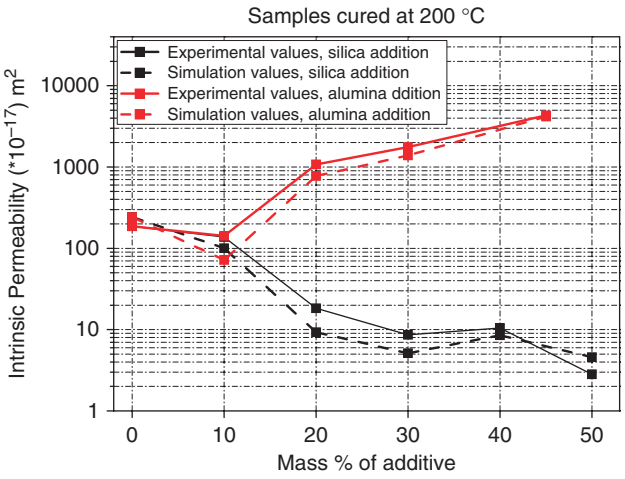

Fig. 11. Comparison of experimental and simulation values of intrinsic permeability with silica or alumina additions in samples cured at 200°C.

available for download at ftp://ftp.nist.gov/pub/BFRL/bentz/permsolver. This method has been used previously,[35] for pervious concrete for example, but we believe that this study is the first time that it has been used to compute permeability for hydrothermal and oilwell cement systems. Similar approaches can be applied to compute other properties, such as electrical conductivity or ionic diffusion, of the 3-D reconstructed microstructures.[32,35]

We have computed the permeabilities of samples cured at 200° and 350°C with silica or alumina additions. The results in Figs. 11 and 12 show that the experimental and simulation values are in good agreement. Therefore, we conclude that the 3-D models used to compute permeability represent well the characteristics of the real microstructures that control liquid transport. All the results present in Figs. 11 and 12 are simulation values of permeabilities calculated on the x direction of the model. In a few samples, the permeability has been computed in the other two directions (y and z) and the results are very similar, suggesting that both the 3-D model and the real microstructure are isotropic.

IV. Conclusions

In this paper, we have discussed the engineering properties of hydroceramic materials cured at 200°–350°C and the relationship of these properties with microstructure and the evolution of various minerals. In addition, computed permeabilities have been compared with experimental results. Our main conclusions are summarized as follows:

(1) By adding more than 20% of silica flour, the engineering properties of the hydroceramics are improved due to the formation of xonotlite, gyrolite, or truscottite. The property values of these materials are within the API specifications for very deep oil or geothermal well sealants.

(2) Adding more than 20% of alumina at 200° and 250°C, results in the formation of hydrogarnets, which decrease the engineering properties of the hydroceramics as they create highly porous microstructures.

(3) At 300° and 350°C when adding alumina, calcium aluminum silicate hydrate and bicchulite grow between the hydrogarnet aggregates, improving permeability, with values lying within the acceptable limits of the API specification. On the other hand, the compressive strength values of these materials are very low and outside of the API specification.

(4) Adding both silica and alumina to the system, results in samples that contain high amounts of xonotlite, gyrolite, 11 Å tobermorite, or truscottite, which have improved engineering properties.

(5) The simulation values of permeability are in good agreement with the experiments, demonstrating the potential of a computational image-based approach as an alternative to time-consuming experimental measurements of permeability. Ultimately, such simulations could be used to support the design of cement systems.

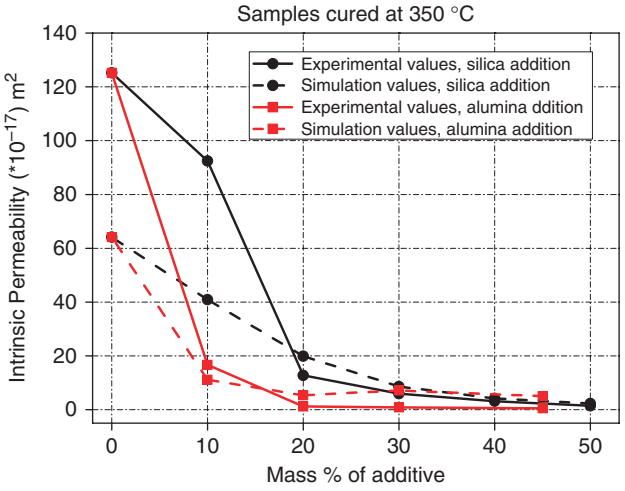

Fig. 12. Comparison of experimental and simulated values of intrinsic permeability with silica or alumina additions in samples cured at 350°C.

Acknowledgments

We thank Chris Jeffree for expert help with the scanning electron microscope, and Margaret Carter for expert help with permeability measurements. We also thank Dyckerhoff and Sibelco for donating starting materials.

References

[1]E. B. Nelson, "Thermal Cements"; pp. 9/1–19 in *Well Cementing*, Edited by E. B. Nelson. Schlumberger Educational Services, Sugar Land, TX, 1990.
[2]A. J. Philippacopoulos and M. L. Berndt, "Structural Analysis of Geothermal Well Cements," *Geothermics*, **31** [6] 657–76 (2002).
[3]R. A. Kennerly, "Products of Hydrothermal Hydration of Cements from Geothermal Bores," *N. Z. J. Sci.*, **4**, 453–68 (1961).
[4]H. F. W. Taylor, *Cement Chemistry*, 2nd edition, Thomas Telford Publishing, London, 1997.
[5]R. Oberste-Padtberg, "Degradation of Cements by Magnesium Brines–A Microscopic study"; pp. 24–36 in *Proceedings of the 7th International Conference on Cement Microscopy*, Edited by J. Bayles, G. R. Gouda, and A. Nisperos. International Cement Microscopy Association, Fort Worth, TX, 1985.
[6]T. Sugama, L. E. Brothers, and T. R. Van de Putte, "Air-Foamed Calcium Aluminate Phosphate Cement for Geothermal Wells," *Cem. Concr. Comp.*, **27** [7–8] 758–68 (2005).
[7]N. Meller, C. Hall, and J. Phipps, "A New Phase Diagram for the $CaO–Al_2O_3–SiO_2–H_2O$ Hydroceramic System at 200°C," *Mater. Res. Bull.*, **40**, 715–23 (2005).
[8]N. Meller and C. Hall, "Hydroceramic Sealants for Geothermal Wells"; pp. 281–4 in *Proceedings of the International Congress on Applied Mineralogy*, Edited by M. Pecchio, F. R. D. Andrade, L. Z. D. D'Agostino, H. Kahn, L. M. Sant'Agostigno, and M. M. M. L. Tassinari, International Council for Applied Mineralogy, Águas de Lindóia, Brazil, 2004.
[9]N. Meller, C. Hall, K. Kyritsis, and G. Giriat, "Synthesis of Cement Based $CaO–Al_2O_3–SiO_2–H_2O$ (CASH) Hydroceramics at 200 and 250°C: Ex-Situ and In-Situ Diffraction," *Cem. Concr. Res.*, **37**, 823–33 (2007).
[10]N. Meller, K. Kyritsis, and C. Hall, "The Mineralogy of the $CaO–Al_2O_3–SiO_2–H_2O$ (CASH) Hydroceramic System from 200° to 350°C," *Cem. Concr. Res.* **39** [1] 45–53 (2009).
[11]L. D. Sanders and W. J. Smothers, "Effect of Tobermorite on the Mechanical Strength of Autoclaved Portland Cement–Silica Mixtures," *J Am. Concr. Inst.*, **28**, 127–34 (1957).
[12]E. Grabowski and J. E. Gillott, "Modifications of Engineering Behaviour of Thermal Cement Blends Containing Silica Fume and Silica Flour by Replacing Flour with Silica Sand," *Cem. Concr. Res.*, **19** [4] 499–508 (1989).
[13]G. Carter and D. K. Smith, "Properties of Cementing Compositions at Elevated Temperatures and Pressure," *Trans. Metall. Soc. Am. Inst. Metall. Eng.*, **213** [2] 20–6 (1958).
[14]E. L. White, C. A. Langton, M. W. Grutzeck, and D. M. Roy, "High Temperature Cements for Geothermal Applications," *Am. Ceram. Soc. Bull.*, **58** [3] 334 (1979).
[15]N. Isu, K. Sasaki, H. Ishida, and T. Mitsuda, "Mechanical Property Evolution During Autoclaving Process of Aerated Concrete Using Slag. 1. Tobermorite Formation and Reaction Behaviour of Slag," *J. Am. Ceram. Soc.*, **77** [8] 2088–92 (1994).

[16]M. L. Berndt and C. E. Mancini, "Tensile Tests on Plain and Fibre Reinforced Geothermal Cements," *J. Mater. Sci.*, **39** [5] 1727–33 (2004).
[17]J. B. Odelson, E. A. Kerr, and W. Vichit-Vadakan, "Young's Modulus of Cement Paste at Elevated Temperatures," *Cem. Concr. Res.*, **37** [2] 258–63 (2007).
[18]G. L. Kalousek and S. L. Chow, "Research on Cements for Geothermal and Deep Oil Wells," *Soc. Petrol. Eng. J.*, **16** [6] 307–9 (1976).
[19]API Specification 10. *Specification for Materials and Testing for Well Cements.* American Petroleum Institute, Washington, DC, 1982.
[20]ASTM Annual Book of Standards C39. *04.02 Compressive Strength of Cylindrical Concrete Specimens.* American Society for Testing and Materials, Philadelphia, 1999.
[21]G. W. Scherer, "Measuring Permeability of Rigid Materials by a Beam-Bending Method: I, Theory," *J. Am. Ceram. Soc.*, **83** [9] 1612–3 (2000).
[22]G. W. Scherer, J. J. I. Valenza, and G. Simmons, "New Methods to Measure Liquid Permeability in Porous Materials," *Cem. Concr. Comp.*, **37** [3] 386–97 (2007).
[23]API Specification 10. *Recommended Practices for Core Analysis.* American Petroleum Institute, Dallas, 1998.
[24]M. Sosoro, W. D. Hoff, and M. A. Wilson, "Penetration and Permeability of Concrete: Barriers to Organic and Contaminating Liquids"; pp. 187–212 in *Testing Methods*, Edited by H. W. Reinhardt. E&FN Spon, London, 1997.
[25]L. J. Buckley, M. A. Carter, M. A. Wilson, and J. D. Scantlebury, "Methods of Obtaining Pore Solution from Cement Pastes and Mortars for Chloride Analysis," *Cem. Concr. Res.*, **37** [11] 1544–50 (2007).
[26]C. Hall and W. D. Hoff, *Water Transport in Brick, Stone and Concrete.* Spon Press, London, 2002.
[27]K. M. Green, W. D. Hoff, M. A. Carter, M. A. Wilson, and J. P. Hyatt, "A High Pressure Permeameter for the Measurement of Liquid Conductivity of Porous Construction Materials," *Rev. Sci. Intrum.*, **70** [8] 3397–401 (1999).
[28]E. Grabowski and J. E. Gillott, "Effect of Replacement of Silica Flour with Silica Fume on Engineering Properties of Oilwell Cements at Normal and Elevated Temperatures and Pressures," *Cem. Concr. Res.*, **19** [3] 333–44 (1989).
[29]L. H. Eilers, E. B. Nelson, and L. K. Moran, "High-Temperature Cement Compositions: Pectolite, Scawtite, Truscottite or Xonotlite: Which Do you Want?" *J. Pet. Technol.*, **35** [8] 1373–7 (1983).
[30]E. B. Nelson and L. H. Eilers, "Cementing Steamflood and Fireflood Wells — Slurry Design," *J. Can. Pet. Technol.*, **25** [5] 58–63 (1985).
[31]K. Luke, H. F. W. Taylor, and G. L. Kalousek, "Geothermal Well Cements — Formation of Truscottite, Xonotlite and Scawtite," *Am. Ceram. Soc. Bull.*, **58** [3] 334 (1979).
[32]D. P. Bentz and N. S. Martys, "Hydraulic Radius and Transport in Reconstructed Model Three-Dimensional Porous Media," *Transp. Porous Media*, **17** [3] 221–38 (1994).
[33]D. P. Bentz and N. S. Martys, "A Stokes Permeability Solver for Three-Dimensional Porous Media," 2007. NISTIR 7416, U.S. Department of Commerce,
[34]N. S. Martys, S. Torquato, and D. P. Bentz, "Universal Scaling of Fluid Permeability for Sphere Packings," *Phys. Rev. E*, **50** [1] 403–8 (1994).
[35]D. P. Bentz, "Virtual Pervious Concrete: Microstructure, Percolation, and Permeability," *ACI Mater. J.*, **105** [3] 297–301 (2008). □